JGR Space Physics

RESEARCH ARTICLE
10.1029/2024JA032678

Effect of Vertical Shear in the Zonal Wind on Equatorial Electrojet Sidebands: An Observational Perspective Using Swarm and ICON Data

J. Sreelakshmi[1,2], Astrid Maute[3,4], Arthur D. Richmond[2], Geeta Vichare[1], Brian J. Harding[5], and Patrick Alken[3,6]

[1]Indian Institute of Geomagnetism, Navi Mumbai, India, [2]High Altitude Observatory, National Centre for Atmospheric Research, Boulder, CO, USA, [3]Cooperative Institute for Research in Environmental Sciences, University of Colorado, Boulder, CO, USA, [4]Space Weather Prediction Center, NOAA, Boulder, CO, USA, [5]Space Sciences Laboratory, University of California, Berkeley, CA, USA, [6]National Center for Environmental Information, NOAA, Boulder, CO, USA

Key Points:

- First observational evidence of effect of zonal wind gradients at ∼130–180 km on low-latitude Equatorial Electro-Jet sideband currents
- The altitude variation of the zonal wind gradient modulates the latitudinal variation of EEJ sideband currents
- With increasing westward wind shear, the strength of low-latitude Equatorial Electro-Jet sideband current increases

Supporting Information:

Supporting Information may be found in the online version of this article.

Correspondence to:

J. Sreelakshmi,
sreelaxmij@gmail.com

Citation:

Sreelakshmi, J., Maute, A., Richmond, A. D., Vichare, G., Harding, B. J., & Alken, P. (2024). Effect of vertical shear in the zonal wind on equatorial electrojet sidebands: An observational perspective using Swarm and ICON data. *Journal of Geophysical Research: Space Physics*, *129*, e2024JA032678. https://doi.org/10.1029/2024JA032678

Received 21 MAR 2024
Accepted 12 SEP 2024

Abstract The wind dynamo in the ionosphere leads to differential motion of ions and electrons, which in turn sets up electric fields and currents. Observations show that daytime lower thermospheric horizontal winds have large vertical gradients. Numerical modeling conducted approximately 50 years ago demonstrated that the zonal wind shears in the ∼130–180 km altitude range can generate off-equatorial relative minima (dips) in the daytime height-integrated eastward current density, appearing as westward sidebands north and south of the equatorial electrojet (EEJ). This study observationally confirms this connection for the first time by combining Ionospheric CONnection explorer zonal wind profiles and Swarm latitudinal zonal currents. We demonstrate observationally that the magnitude of the EEJ sideband current is proportional to the strength of westward turning winds with altitude in the Pedersen conductivity dominated region. Additional numerical experiments explain the importance of wind shear in different altitude regions in generating the sideband current. This study contributes to the better understanding of the neutral wind effect on the local current generation.

Plain Language Summary The winds in the E-region ionosphere push the plasma in the presence of Earth's magnetic field, causing ions and electrons to move separately, producing electric current. The low-latitude ionospheric current system consists of an intense eastward current at the magnetic equator (called Equatorial Electro-Jet (EEJ)) and off-equatorial reduced eastward or relative westward currents (EEJ sideband currents) in both hemispheres. Modeling studies have shown that the altitudinal gradient of the zonal wind is related to the strength of the EEJ sideband currents. However, observational studies to validate these results have been missing to this date. This study utilizes simultaneous observations from Ionospheric CONnection explorer and Swarm satellites to provide insights on the connection between low-latitude winds and currents, which will improve our understanding of the causes of daytime ionospheric variability.

1. Introduction

The equatorial electrojet (EEJ) is an enhancement of the eastward current in the dayside E-region at the magnetic equator, considerably stronger than the normal large-scale daytime low-latitude eastward ionospheric currents. Studies of the latitude structure of EEJ magnetic perturbations, using magnetometer chains on the ground (Fambitakoye & Mayaud, 1976a, 1976b; Fambitakoye et al., 1976) or satellite magnetometers at low-Earth Orbiting (LEO) altitudes (Cain & Sweeney, 1973; Lühr et al., 2004; Zhou et al., 2018), have found that the height-integrated eastward current density not only peaks at the magnetic equator but also frequently shows local minima in strength around roughly ±5° magnetic latitude. The present study investigates the source of these current reductions, which we shall refer to as EEJ sideband currents.

Richmond (1973) developed a physical model of EEJ and demonstrated that the effect of height-varying winds is largest on the currents at off-equatorial latitudes. Using this model, Fambitakoye et al. (1976), abbreviated by F76 hereafter, demonstrated that the zonal wind shear in the altitude regions where Pedersen conductivity dominates (∼130–180 km) is responsible for the reduction in eastward currents at low-latitudes. Reddy and Devasia (1981) also found that the vertical shears of the zonal winds can generate currents which dominate at the off-equatorial latitudes. Fang et al. (2008) used TIEGCM simulations to examine the influence of neutral winds in different

altitude regions on the equatorial upward E × B drift and the ground magnetic perturbations. Their Figure 4 shows a schematic representation of the study done by Fambitakoye et al. (1976).

Until recently, there were no simultaneous observations of wind in the lower thermospheric altitudes (~90–200 km) along with the height-integrated current density to observationally evaluate the effect of the height variation of the zonal wind on the sideband currents as suggested by F76. With the recent availability of wind observations from the MIGHTI (Michelson Interferometer for Global High-Resolution Thermospheric Imaging, Englert et al., 2017) instrument on the ICON (Ionospheric CONnection explorer, Immel et al., 2018) spacecraft, together with low-latitude current estimates from the Swarm spacecraft (Friis-Christensen et al., 2006), this hypothesis can now be tested. That is the primary purpose of this paper. After almost 50 years, there is a unique opportunity to inspect the effect of zonal wind shears on low-latitude sideband currents using the wind measurements from ICON and EEJ derived from observations by the Swarm satellites.

In order to understand how the winds generate currents in the ionosphere in general, a brief overview of the ionospheric electrodynamics is given. In the ionospheric E region, the thermospheric neutral winds push the ionospheric plasma in the presence of Earth's magnetic field, causing differential motion of ions and electrons, which results in wind dynamo currents. The current system is divergence-free and hence polarization electric fields and currents are established. This current system produced by the dynamo action of a non-storm-time wind system is called Solar quiet currents (Sq) flowing in the low-to-mid latitudes and along geomagnetic-field lines between the southern and northern magnetic conjugate points.

The ionospheric current density **J** can be expressed using Ohm's Law as follows:

$$\mathbf{J} = \hat{\sigma} \cdot (\mathbf{E} + \mathbf{U} \times \mathbf{B}) \tag{1}$$

Here, $\hat{\sigma}$ is the conductivity tensor, **E** is the electric field, **U** is the neutral wind, and **B** is the ambient magnetic field. The three different conductivities are the parallel (or direct) ($\sigma_{\parallel}$), the Pedersen (σ_P), and the Hall conductivity (σ_H). Parallel conductivity is parallel to **B** and Pedersen and Hall conductivities are perpendicular to **B** and with currents flowing parallel and perpendicular to the electric field, respectively. We assume equipotential field lines since the parallel conductivity is several orders of magnitude greater than the perpendicular conductivities. Accordingly, ionospheric electric fields and currents are strongly organized by the geomagnetic field. During sunlit hours the Pedersen and Hall conductivities are largest at altitudes of 90–200 km, the so-called "dynamo region," where significant current can flow perpendicular to **B**.

At low latitudes, the zonal component of the electric current in ionosphere mostly flows eastward during daylit hours. At the magnetic equator, the east-west component of the equatorial electric field (EEF) and the horizontal geometry of magnetic fields, along with the non-conducting atmosphere below ~80 km, leads to an effective zonal ionospheric conductivity, known as Cowling conductivity (Cowling effect, Chapman, 1956). This results in EEJ, which generally peaks around ~105 km altitude. The EEJ is accompanied by a northward magnetic perturbation at the ground and a southward perturbation at LEO spacecraft altitudes.

We want to note that it is a long-standing debate whether EEJ should be considered part of Sq or not (Onwumechili, 1992; Stening, 1995; Vichare et al., 2016; Yamazaki & Maute, 2017), but this distinction is not discussed in the present study. In this study we focus on the off-equatorial eastward current (i.e., ~5° off the magnetic equator) which can be reduced or even reversed (as shown by simulations, Anandarao & Raghavarao, 1987; Richmond, 1973) with day-to-day variations similar to the EEJ (Jadhav et al., 2002; Thomas et al., 2017; Zhou et al., 2018).

In observations, Sq and EEJ current are intermixed and therefore need to be separated if studying one of them. Lühr et al. (2004) used a second-degree spherical harmonic polynomial to separate the Sq current signal from the EEJ. The resulting magnetic signal exhibits shoulders on either side of the negative scalar magnetic field associated with the EEJ current itself. It should be noted here that the negative deflection is only true for magnetic records above the E region currents. When inverted to zonal current, these shoulders can be seen as relative westward current dips in the sheet current density (see Figure 3 of Lühr et al. (2004)).

There are some satellite-based studies on the sideband currents seen at the flanks of the magnetic equator. However, to our knowledge, there is only one ground-based study conducted by Fambitakoye and Mayaud (1976a, 1976b) in this domain as it is difficult to establish and maintain a sufficiently dense chain of

ground magnetometers. The ground-based magnetometer network has become denser over the past five decades. However, the spatial coverage provided by LEO satellites is unparalleled compared to ground observatories. Satellites can cover every latitude in the low-to-equatorial regions, which is crucial for estimating sideband currents. Cain and Sweeney (1973) found high "shoulders" at off-equatorial latitudes in the residual of total magnetic field observations made by the POGO satellite, indicating the presence of sideband currents. Lühr et al. (2004) deduced the horizontal distribution of height-integrated current densities (I) from the CHAMP satellite residual magnetic field measurements, parameterizing the meridional current profile by 81 zonally oriented line currents around the EEJ peak. They found that the sideband currents are a common feature peaking on average at ±5° magnetic latitude, although they also found that the sideband amplitude is sensitive to how diamagnetic plasma effects are calculated. Note that Maute and Richmond (2017) and Sreelakshmi and Vichare (2020) found that correcting only for magnetic perturbations due to pressure-gradient currents (diamagnetic effects) without including effects of gravity-driven currents may increase rather than decrease the errors. Recently, Zhou et al. (2018) comprehensively characterized the low-latitude sideband currents using 5 years of CHAMP magnetic data. They deduced the average sideband current characteristics (e.g., intensity, the latitude of peak) and its dependencies on local time, season, and solar activity.

The reversal of EEJ either due to a reversal of EEF or due to zonal winds is commonly known as Counter Electrojet or CEJ. Yamazaki et al. (2021) used simultaneous observation of EEJ magnitude derived from magnetic observations by the Swarm satellite missions and horizontal winds derived from ICON/MIGHTI observations to inspect the effect of local zonal winds on EEJ and CEJ. Their results suggest that the vertical profile of the equatorial zonal wind can modulate the equatorial electric field and may lead to the reversal of the EEJ. On average during CEJ events, winds are found to be eastward and westward around ∼110 and ∼140 km, respectively, while the reverse is true for EEJ.

Thermospheric winds vary with height, latitude, longitude, and time. Solar heating produces large-scale daily variations in the winds, with amplitudes that tend to increase with altitude above approximately 120 km, according to modeling studies (Forbes, 2007). Upward-propagating tides from the lower atmosphere strongly influence the winds below 120 km (Hagan & Forbes, 2002) but tend to dissipate at higher altitudes. These tides can vary with latitude more rapidly than the solar-produced winds above 130 km, but generally do not vary with latitude as rapidly as the currents comprising the Equatorial Electrojet and its sidebands. Gravity waves can have latitude scales comparable to the EEJ and its sidebands, but these waves are irregular and cannot produce consistent structures in the ionospheric currents. Therefore, it is unlikely that the latitude structure of the winds can be directly responsible for the presence of sideband currents. However, the modeling study by F76 showed that vertical shear of the zonal wind, especially in the 130–180 km altitude range, can produce sidebands similar to those observed by magnetometers, without requiring latitude variations of the wind. Therefore, we focus on the effects of vertical structure, which is better observed.

Observations clearly show that neutral winds in the thermosphere are highly variable and have large vertical shears (England et al., 2022; Shepherd et al., 1993, 2012). Since the winds in the lower ionosphere (100–200 km) are sparsely sampled, the present study could inform estimates of the wind from magnetometer measurements, which are more dense than wind measurements (Alken et al., 2008). In addition, Richmond's (1973) model of EEJ is used in this study to investigate the importance of wind shear in different altitudinal regions using ICON/MIGHTI winds and Swarm EEF.

Section 2 outlines the data on low-latitude currents from Swarm, zonal winds observed by ICON, and the EEJ model utilized in this study. It also covers the data selection process, methodology, and the associated errors and uncertainties. Section 3 features scatter plots with gradient of zonal winds with sideband currents, both for individual measurements and for the mean values of each variable based on data grouped according to either variable. The section also includes a discussion with two linear regression lines with one of the variable as the independent variable. The impact of the altitudinal dependence of the zonal wind gradient on sideband currents is discussed in Section 4, and conclusions are presented in Section 5.

2. Data and Model

2.1. Low-Latitude Currents Observed by the Swarm Satellite Mission

Swarm (Friis-Christensen et al., 2006; Olsen et al., 2013) is a constellation of three polar LEO satellites (A, B, and C) launched on 22 November 2013. All three satellites have an inclination of approximately ∼87°. Swarm A and C are flying side-by-side with a longitudinal difference of ∼1.4° at the equator at an altitude of ∼450 km, while Swarm B is orbiting at a higher altitude of ∼510 km. We use the Swarm level-2 EEF data product (Alken, Maus, et al., 2013), which gives the EEJ variations and eastward EEF estimates. Detailed information on the retrieval of EEJ from magnetic field measurements can be found in Alken (2020). The global Sq and unmodeled magnetospheric field are assumed to be represented by a magnetic scalar potential defined in a spherical coordinate system, which is fitted orbit-by-orbit to data between ±(12°–45°) quasi-dipole (QD) latitude and then subtracted from the residual magnetic field. Here the residual magnetic field represents the satellite magnetic field measurements with internal (core and lithospheric) and magnetospheric contributions subtracted using the CHAOS-7.15 model (Finlay et al., 2020). No corrections are made for F-region currents associated with gravitational and pressure-gradient forces on the plasma, unlike the study of Lühr et al. (2004) that corrected for diamagnetic effects associated with plasma pressure gradients. Further, the remaining magnetic field perturbations are inverted to height-integrated magnetic-eastward current densities as described in Alken (2020).

2.2. Zonal Winds Observed by ICON/MIGHTI

ICON (Immel et al., 2018) is a low-latitude satellite launched on 11 October 2019 at an altitude of ∼600 km. The satellite orbits at an inclination of 27°, with a latitudinal coverage from about 12°S to 40°N. As ICON is a low-inclination satellite, it flies through all local times during every orbit. The MIGHTI (Englert et al., 2023) instrument onboard ICON measures Doppler shifts in naturally occurring atomic oxygen airglow emissions to estimate the neutral wind velocity. We use the version 4 of Level 2.2 data product derived from the green-line emission at 557.7 nm wavelength (Harding et al., 2017, 2023). For this study, we use geographic zonal wind observations in the height range of 95–200 km. Harding et al. (2021) validated the green-line wind data against ground meteor radar data.

2.3. Data Selection and Methodology

We select coincident observations of Swarm and ICON/MIGHTI during geomagnetically quiet days with (a) Kp ≤ 3+ and between January 2020 and February 2022. Figures 1a and 1b display the 10.7 cm solar radio flux (Tapping, 2013) and Kp index (Matzka et al., 2021) for the study period. Since solar flux was below 100 sfu for most days, it is not a criterion for our data selection. The geomagnetic activity is quite low for most of the time period.

In order to decide whether segments of orbits from the spacecraft are sufficiently close in space and time to constitute a conjunction we use the central times and locations of these segments. The other selection criteria are as follows: (b) ICON wind measurements should be within ±30 min of Swarm equatorial measurements, and (c) the longitude of ICON wind measurements should be within ±10° of the longitude of the Swarm satellite at the magnetic equatorial crossing. Manoj et al. (2006) reported that beyond 15° longitudinal separation, the correlation between EEJ intensities at the two locations is statistically insignificant. (d) The wind is measured within ±5° of the magnetic equator. (e) Only high quality wind data is chosen (wind quality factor = 1). (f) Data is chosen between 9 and 15 local time (LT). Even though there are local time and longitudinal variations in Equatorial Electrojet due to geomagnetic main field and neutral winds (Alken, Chulliat, & Maus, 2013; Lühr et al., 2021; Yamazaki et al., 2017), the local time window is chosen wide enough to have adequate number of conjunctions. If multiple wind profiles meet all the criteria (a–f) for a given EEJ observation, we use the average of the wind profiles.

We select EEJ data with height-integrated current density (I_{eq}) at the magnetic equator, of $I_{eq} \geq 25$ mA/m, to avoid the influence of weak EEJ which does not have well developed sideband currents (Thomas et al., 2017). Applying all the data selection criteria, we obtained 572, 520, and 549 conjunctions between ICON and Swarm A, B, and C, respectively. It should be noted that the westward sideband currents are sensitive to the details of the procedure for Sq removal. Therefore, the following provides a detailed description of the method used to derive the zonal current based on Swarm magnetic field data.

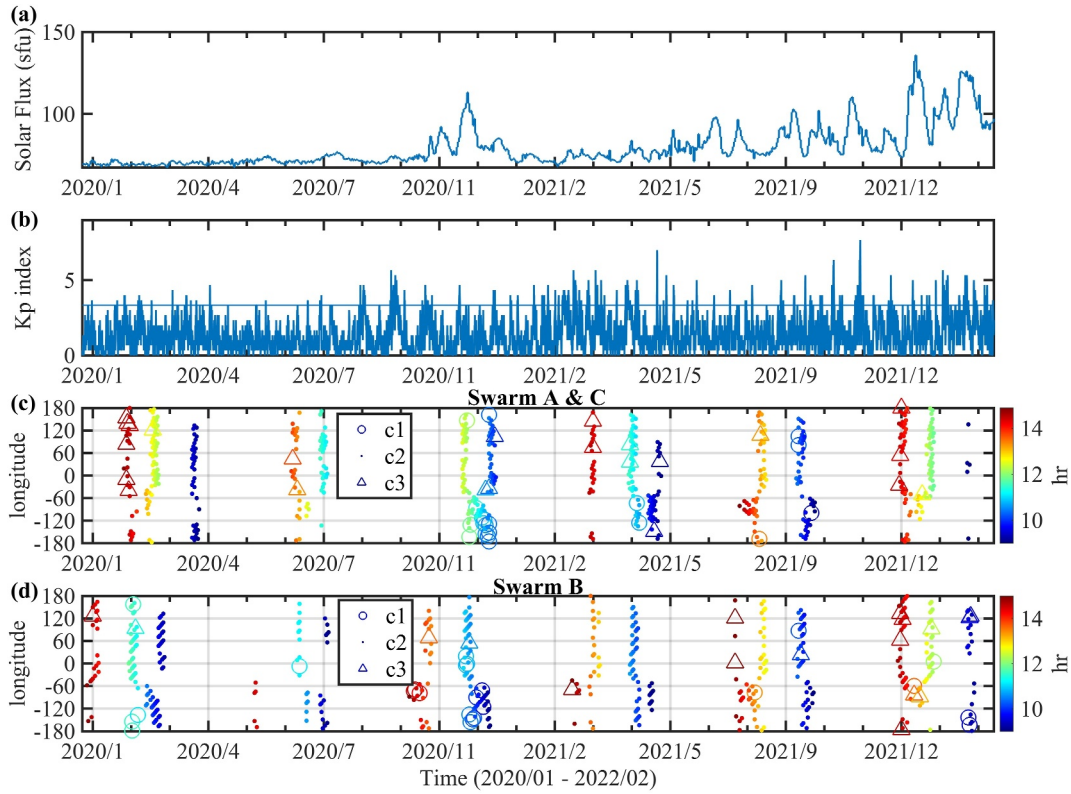

Figure 1. (a) Solar activity index, 10.7 cm solar flux in sfu (solar flux units), (b) Kp index, (c) longitude of Swarm A and C in conjunction with ICON/MIGHTI, and (d) longitude of Swarm B in conjunction with ICON/MIGHTI during the period 1 January 2020–11 February 2022. Different symbols in (c) and (d) indicate different categories C1–C3 based on the minimum sideband current densities as described in the text, and the color indicates the local time in hours.

Figure 2a illustrates the determination of the eastward current density (EEJ) from the residual magnetic field obtained from Swarm A on 01 December 2020, at 22:47 UT (longitude = 196.74°E, LT = 11:54). The solid blue line represents the residual magnetic field (which is the raw measurement minus the magnetic fields from core, lithosphere, and symmetric magnetospheric fields, as described above), while the contribution from Sq and unmodeled magnetospheric ring current fields (referred to as Sq') is depicted by the blue dashed line. The latter is

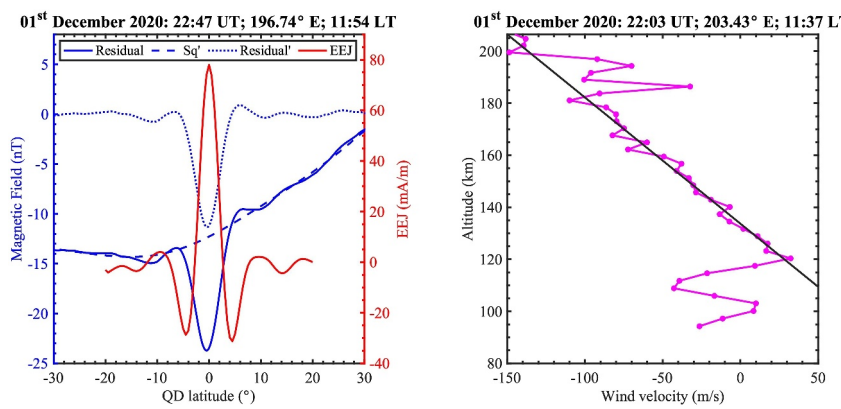

Figure 2. (a) Left *Y*-axis shows the residual magnetic field (solid blue line), Sq': magnetic field due to Sq and unmodeled magnetospheric currents (blue dashed line) and Residual' (blue dotted line): representing the difference between residual magnetic field and Sq'. The right *Y*-axis illustrates the Equatorial Electrojet in mA/m (red line) (b) Altitudinal variation of zonal wind velocity in m/s, with the black line representing the least-squares line fitted to wind velocity between the altitudes 130 and 180 km.

subtracted from the former to obtain the Residual' shown as a blue dotted line. The magnetic field contribution from Sq currents and unmodeled magnetospheric currents is estimated by fitting a model to scalar magnetic residuals, with Sq field and its induced counterparts represented by a magnetic scalar potential for sources internal to the satellite orbit, and an external scalar potential defined for magnetospheric currents.

The height-integrated EEJ current density derived from the Residual' (magnetic field after subtracting Sq' contributions from the residual magnetic field) is also shown in red line in the figure. The minima I_{off} of the current density within ±(3–9)° of the magnetic equator represent the sideband currents (Zhou et al., 2018). We neglect any data with an absolute difference in northern and southern value of I_{off} greater than 15 mA/m.

Figure 2b shows the zonal wind corresponding to the current example of Figure 2a. A least-square fitted line for the zonal wind velocities between 130 and 180 km is shown to visualize the wind behavior minimizing the influence of variability and noise. In our analysis of Swarm-ICON/MIGHTI data pairs we refer to the slope of this line as "Gradient in zonal wind velocity" (ΔU_h). One feature of interest to this study is the fact that the wind tends to be increasingly westward with increasing height above 120 km. According to the modeling results of F76, a wind that is increasingly westward above 135 km will generate height-integrated eastward currents that are stronger 10° away from the magnetic equator compared to 5° away from the equator. This contributes to the creation of a sideband-like feature in the latitudinal current profile, when added to the enhanced EEJ current driven by the EEF that F76 shows to lie mostly equatorward of 5°. The results of F76 also indicate that winds below 135 km have little effect on the difference of current between 5° and 10° magnetic latitude and therefore are not expected to have much influence on the strength of sideband currents. However, it should be noted that these low-altitude winds do affect the difference of current between 10° and the equator and therefore can influence the EEJ peak current relative to the background Sq current level.

2.4. Data Errors and Uncertainties

Instrumental errors are relatively small, both for the Swarm magnetometer (<0.3 nT (Friis-Christensen et al., 2006)) and for the ICON/MIGHTI wind data (<10 ms^{-1} (Harding et al., 2017)). However, there are considerable uncertainties in estimating sideband current strengths from the magnetometer data and in using the ICON/MIGHTI observations to estimate the magnetic-eastward wind at the precise time and location of the paired Swarm data. These uncertainties can be considered types of data errors or measurement errors when further analyzing the paired conjunction data and their correlation.

One uncertainty is that the presence and magnitude of sideband currents may be overestimated by the fitting procedure. For instance, the fact that the Residual' is forced toward 0 nT at low latitude region poleward of ±12° QD latitude (see Figure 2a) means that any negative magnetic field perturbation produced there by the eastward EEJ must be offset by positive contributions from sideband currents on either side of the eastward EEJ. Furthermore, magnetic perturbations on the horizontal scale of the sideband currents (corresponding roughly to a horizontal wavelength of ∼10° or ∼1,200 km) decay with height above the main current layer at ∼110 km altitude. The decay follows an exponential distance scale of ∼200 km, calculated as 1,200 km/2π. Considering the Swarm satellite's orbit at an altitude of approximately 340 km above the EEJ, the magnetic perturbation diminishes to approximately 1/6 compared to its intensity just above the E-region currents. Consequently, it becomes evident that other factors, such as unresolved or unmodeled sources contributing to the residual magnetic field, may introduce signals comparable in magnitude to the sideband signal. Among the unmodeled sources are the effects of F-region pressure-gradient and gravity-driven currents. Therefore, accurately extracting the relatively weak effects of sideband currents from the Swarm magnetic data is subject to considerable uncertainty. It is difficult to quantify the magnitudes of this uncertainty and the potential bias in the magnitude of the sideband currents.

Because the times and locations of ICON/MIGHTI wind data differ somewhat from the times and locations of the Swarm observations, the wind observations differ from the true winds at the Swarm locations. Currently, we lack good quantitative information about the variability of the winds on the temporal and spatial scales of our data-selection procedure. However the difference between the observed and true winds at Swarm locations is likely a non-negligible fraction of our selected wind data. Additional wind error comes from our use of the geographic zonal wind to approximate the magnetic-zonal wind which is also affected by geographic meridional winds when the geomagnetic declination is significant.

2.5. EEJ Model

Richmond (1973) describes a physical model of EEJ, which includes neutral winds and two-stream instability. The main assumptions in this model are that (a). Longitudinal gradients of all quantities are negligible, which is a reasonable approximation around ±3 hr from noon time, (b). Latitudinal gradients of the conductivities and winds are negligible, (c). Electric fields do not affect the electron density, and (d). The electrojet is symmetric about the magnetic equator. The model assumes a flat Earth with parabolic geomagnetic field lines and uniform field strength, for which the tangent of the inclination angle is twice the tangent of the magnetic latitude. Given a zonal neutral wind profile, a zonal electric field, and conductivity profiles, the model computes the latitude distribution of height-integrated current, from which I_{off} can be derived. See Richmond (1972, 1973) for further details on the model.

We use the EEJ model in the following to verify that the model can reproduce the observed behavior and to understand how the zonal wind shears at different altitudes contribute to the generation of I_{off}. The wind profiles and EEF obtained from Swarm A and ICON conjunctions for the three different categories are used as input into the EEJ model together with the average solar flux. The currents are estimated during equinox months at 12 LT. The model will produce similar results at solstice conditions since the model does not account for the latitudinal gradients in the wind and conductivity. Above 200 km, we assume that the neutral wind is constant with altitude. We found that the exact variation above 200 km does not influence the I_{off} magnitude. This could be due to either the underestimation of F-region conductivities or the non-inclusion of latitude variations of the conductivity (and wind) in the lower F region in the model.

To be able to compare the model results with the Swarm EEJ data, which has the Sq baseline removed, we subtract a linear baseline from the simulated height-integrated current densities, which is obtained by least-square fitting a line to values between ±(7° and 10°) dip latitude. This procedure is different from that of Swarm data since (a) in the Swarm magnetic data the Sq variation is removed while in the model, a baseline correction in current density is applied, (b) the data is fitted using spherical harmonics versus a linear fit in the model, which is appropriate for the baseline fit, and (c) the fitting procedure on data is between 12° and 45° QD latitude while the model uses values between 7° and 10°.

3. Relating Gradients in Zonal Winds With Sideband Currents

3.1. Scatterplot

Figure 3 shows the sideband current strength I_{off} and wind gradient ΔU_h for every individual pair of conjunctions between Swarm A and ICON for the selected time period. There is considerable scatter, owing to (a) potential measurement errors, especially of the wind; (b) difficulties in separating the signature of ionospheric currents from other current sources; (c) uncertainty in removing Sq currents from EEJ, (d) spatial and temporal variations of the wind and current over the windows used to select conjunctions, and (e) difficulty in determining the gradient of the highly varying altitudinal profile of winds.

Nevertheless, the correlation coefficient of 0.31 is non-negligible. Because the statistical distribution of data points does not appear to represent a normal (Gaussian) distribution, standard measures of statistical significance for this correlation coefficient are not valid. However, the fact that a calculated p value using standard statistical techniques (Witte & Witte, 2017) is extremely small (1.79×10^{-12}) suggests that the correlation is robust. A linear regression line fitted to these data results in a model that statistically can explain 9.61% of the sideband current strength in terms of the wind gradient. As we discuss later, when the data are binned and averaged a larger explained percentage is found for the averaged data.

It is not easy to find an unbiased regression line that might linearly relate I_{off} and ΔU_h, because both of the correlated variables have considerable uncertainty, and because the magnitudes of these uncertainties are not well quantified. If we were to treat one of the variables as independent and without error and then calculate a least-square regression line with the other variable, the resultant slope of the regression line would be under-estimated (Riggs et al., 1978). The slope of the linear regression line when ΔU_h is treated as the independent variable (red dashed line) is ~2.3 As/m and that using I_{off} as the independent variable (yellow line) is ~24.3 As/m. This substantial difference in slopes can be attributed to the impact of measurement errors in the independent variable (known as regression dilution). When ΔU_h is the independent variable, the observed slope is biased toward zero due to the increased variability introduced by measurement errors in ΔU_h. This leads to an

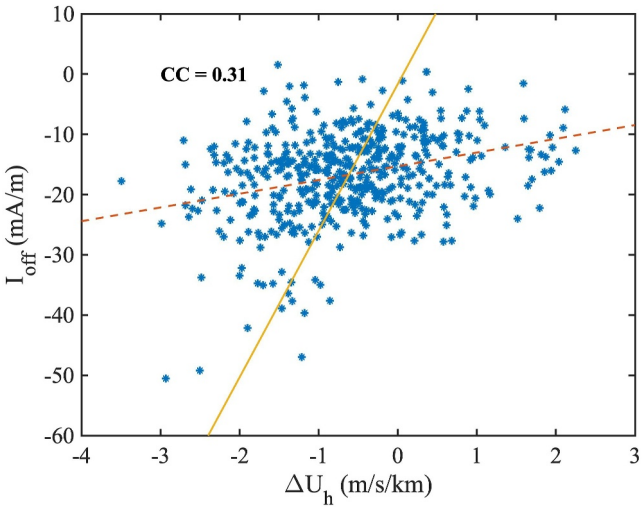

Figure 3. Scatter plot of gradient in ICON/MIGHTI zonal wind velocity with average of I_{off} from Swarm A in northern and southern hemisphere. The correlation coefficient CC is mentioned. Red dashed line indicates linear regression line with ΔU_h as independent variable and yellow line indicate that with I_{off} as independent variable.

underestimation of the true relationship between ΔU_h and I_{off}. Conversely, when I_{off} is treated as the independent variable, the regression model attempts to account for the variability in I_{off}, resulting in a steeper slope. This occurs because the measurement errors in I_{off} cause the regression model to over-compensate, leading to an overestimation of the relationship between the variables. Thus, the observed disparity in the slopes highlights the critical influence of measurement errors on regression estimates, emphasizing the need for careful consideration of these errors. If the ratio of error variances of the two variables were known, it would be possible to calculate an unbiased Deming regression line (Deming, 1964), but we do not yet know the relative error variances. Instead, we explore possible quantitative relations between the winds and sideband currents by analyzing the conjunction data in two different ways: organizing either in terms of I_{off} or in terms of ΔU_h.

3.2. Grouping Data According to Sideband Current Strength

First, we divided the data into three categories based on the minimum height-integrated sideband current density, I_{off} defined by the following conditions for I_{off} in both hemispheres:

$$\text{Category 1} \quad (\text{C1}) : I_{off} <= -30 \text{ mA/m}$$

$$\text{Category 2} \quad (\text{C2}) : -30 < I_{off} <= -5 \text{ mA/m}$$

$$\text{Category 3} \quad (\text{C3}) : I_{off} > -5 \text{ mA/m}.$$

In C1 and C3, we have 20 and 23 conjunctions respectively, for Swarm A with ICON (Figure 1c). Swarm B and C (Figures 1c and 1d) have similar numbers of conjunctions in C1 (24 and 24, respectively) and C3 (17 and 33, respectively). Meanwhile, in C2, the number of conjunctions for the Swarm satellites A, B, and C with ICON is 529, 479, and 492, respectively. The number of conjunctions in category 2 is large compared to the other two categories. Zhou et al. (2018) using CHAMP satellite data found that the sideband currents show a certain dependence on longitude with a variation of 33% between I_{off} at different longitudes. However, Figure 1d shows that the seasonal and longitudinal distribution of the conjunctions is insufficient to be considered as an additional criterion in our analysis.

The first two columns of Figure 4 show the average QD latitudinal profiles of EEJ from Swarm A (left column) and the simultaneous observations of altitudinal variation of zonal winds from ICON/MIGHTI (middle). Each row is for a different category, with C1–C3 from top to bottom. The average EEJ profile shows the largest eastward peak at the magnetic equator with two dips in both hemispheres near ∼5° QD latitude. The average zonal wind is westward in the lower E region from ∼80 to 110 km and then gets less-westward or eastward between ∼110 and 130 km. Above ∼130 km, the wind becomes more westward with altitude.

The magnitude of minimum sideband currents appears to be correlated to the gradient in zonal wind velocity estimated between 130 and 180 km. These altitudes are determined based on the fact that in general during the daytime at low latitude in the 130–180 km region, the Pedersen conductivity is important.

To calculate the altitude gradient of the wind for each category, the zonal wind measurement at each altitude between 130 and 180 km is selected randomly from the individual wind measurements. Then the slope is estimated using the least-square fitting on the selected values. This procedure of random selection and slope estimation is repeated 1,000,000 times and the mean is taken as the final gradient. The standard error $\left(\frac{\text{standard deviation}}{\sqrt{(\text{number of samples})}}\right)$, which shows the variability of the mean of samples is estimated and shown in Figures 4a, 4d, 4g, 4b, 4e, and 4h for the currents and zonal winds. As listed in Table S1 of the Supporting Information S1, I_{off} is −37.26 mA/m for a ΔU_h of −1.64 m/s/km for category C1. For category C2, I_{off} is −15.42 mA/m, and the ΔU_h is −0.65 m/s/km. I_{off} is further reduced to −0.44 mA/m while the ΔU_h is −0.37 m/s/km for category C3. This implies that as the absolute gradient in zonal wind velocity decreases, the sideband current I_{off} decreases. This also

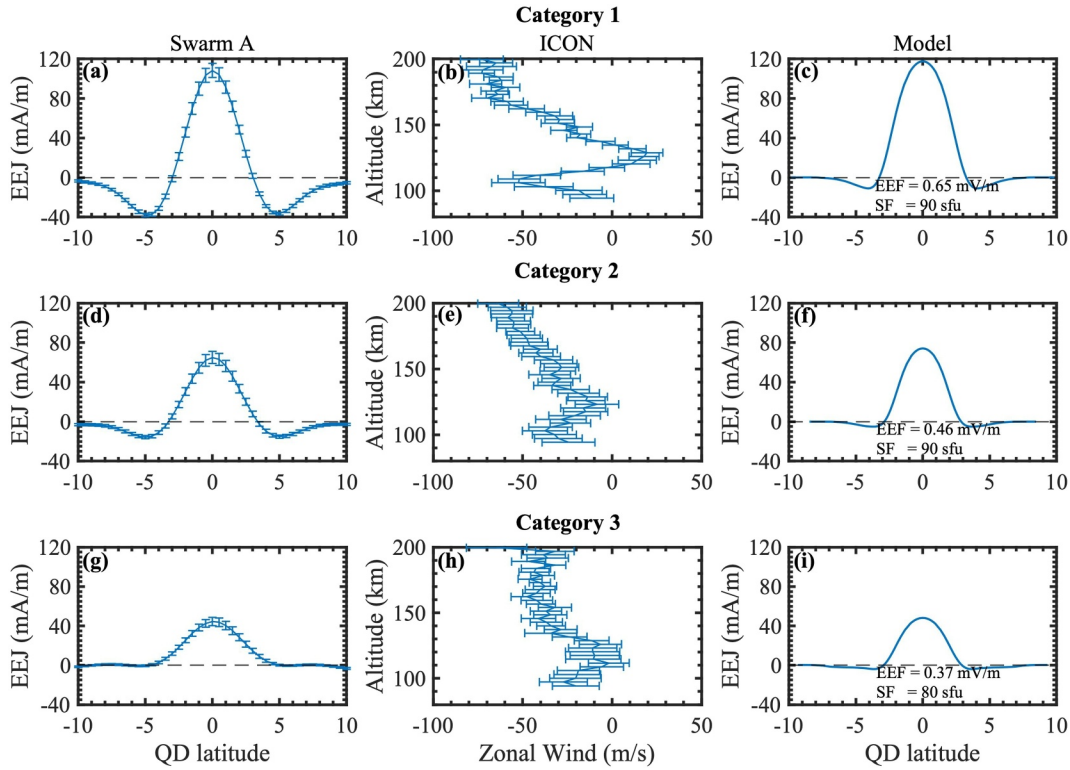

Figure 4. The three columns are average profiles of EEJ from Swarm A, zonal wind from ICON/MIGHTI, and the corresponding EEJ from the model, respectively. This analysis is for grouping of data according to sideband current strength. Swarm EEJ and ICON zonal winds are plotted with standard errors.

indicates that readily available magnetic perturbation data could be used to learn about low-latitude neutral wind height variation.

The third column of Figure 4 illustrates the model results. I_{eq} values are ∼117, 74, 48 mA/m for the EEJ model and ∼108, 65, 44 mA/m for Swarm A for C1, C2, and C3 respectively, matching well but tending to be slightly larger than the measurements. The I_{off} from Swarm are −37.26, −15.42, −0.44 mA/m and from the model are −11, −5, and −3.87 mA/m for C1, C2, C3, respectively. The I_{off} from Swarm is an average from both hemispheres while the model has a symmetric latitudinal variation. The gradient in zonal wind velocity, I_{off} and I_{eq} for the satellites and corresponding model results are summarized in Table S1 of the Supporting Information S1.

3.3. Grouping Data According to Wind Shear

Next, we analyzed the data by grouping it based on altitudinal gradient in zonal winds. The data are categorized based on ΔU_h in 1 m/s/km bins from −3 to 3 m/s/km, resulting in six categories. Figure 5 displays the individual zonal wind measurements from ICON and EEJ from Swarm A for each category. The black line in each figure represents the corresponding mean values. For category 1, I_{off} is −20.86 mA/m for a ΔU_h of −2.32 m/s/km. In category 2, I_{off} is −18.25 mA/m with a ΔU_h −1.44 m/s/km. I_{off} is −15.04 mA/m while the ΔU_h is −0.52 m/s/km for category 3. For the categories 4, 5, and 6, I_{off} is −13.18, −11.69, and −8.00 mA/m for a ΔU_h of 0.39, 1.36, and 2.12 m/s/km, respectively.

As the wind gradient becomes less negative or more positive, the depth of the sideband currents decreases. However, the dependence of I_{off} on ΔU_h appears much less in Figure 5 than one might expect from the relation between I_{off} and ΔU_h seen in Figure 4. Obviously, the manner in which the data are grouped has a strong effect on the derived relation between I_{off} and the wind shear. Nevertheless, the relation is positive in both cases, consistent with a real physical relation.

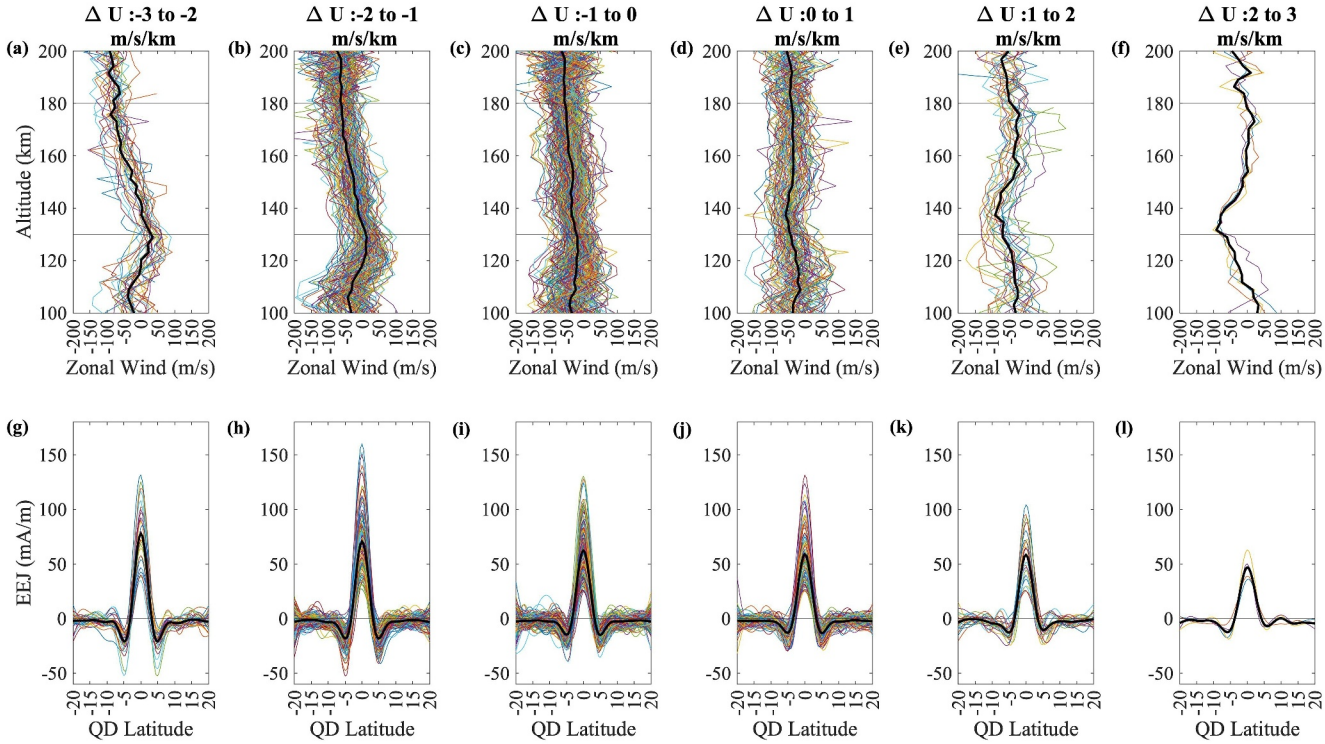

Figure 5. The first row is individual zonal winds from ICON/MIGHTI and second row is EEJ from Swarm A for grouping of data according to wind shear. The black lines in each of the plot show mean Swarm EEJ and ICON zonal winds.

3.4. Linearity of Relation Between I_{off} and ΔU_h

Given the large amount of scatter of the data from individual conjunctions seen in Figure 3, it is not obvious that the data might exhibit a linear relation between I_{off} and ΔU_h, as the physical model would predict. In this section we examine the linearity of the average relation between group-averaged conjunction data.

Figure 6 shows the relation between I_{off} and ΔU_h for data and model, with data from the two groupings described in Sections 3.2 and 3.3. The grouping of data based on I_{off} is termed G1 and that based on ΔU_h is termed G2. The model was driven by G1 group-averaged ICON/MIGHTI data. The different categories from the average conjunctions obtained from Swarm A, B, C and ICON are combined and shown for G1 in orange (solid line) and G2 in magenta (dashed line). The data for G1 was further categorized into five distinct bins with I_{off}: ≤ -30, -30 to -20, -20 to -13, -13 to -5, and >-5 mA/m. This categorization assigns 5 averages of conjunctions for each Swarm satellite A, B, and C, resulting in a total of 15 data points in Figure 6. The figure illustrates that the results for the conjunctions of Swarm B and C and ICON are consistent with the findings using Swarm A and ICON conjunctions. Similarly, G2 also shows the scatter plot of the mean ΔU_h and I_{off} for all six categories for Swarm A, B, and C conjunctions with ICON.

The linear correlation coefficient between I_{off} and ΔU_h is 0.93 and 0.96 for the groups, G1 and G2 respectively, meaning that on average ~86.5%–92.2% of the group-averaged I_{off} variation among the Swarm satellites and among the different cases can be explained by the group-averaged ΔU_h variation using a linear model. It should be noted here that these correlation coefficients and percent explaining variability are only valid for the averaged data in each category in the different groups, and do not necessarily apply to individual conjunctions. The large linear correlation coefficients suggest that the relation between ΔU_h and I_{off} is indeed approximately linear.

The physical model is compatible with the data, considering the differences between the G1 and G2 analyses. The model shows a higher correlation between ΔU_h and I_{off} of 0.98 compared to the observational results. The slope of the linear regression line is ~5.76 As/m for the model (purple dotted line), whereas it is ~24 and ~2.7 As/m for Swarm data based on the groups G1 (orange line) and G2 (magenta dashed line). If the true relation between I_{off} and the wind shear is linear, then the true slope probably lies between the slopes for the G1 and G2 analyses. We

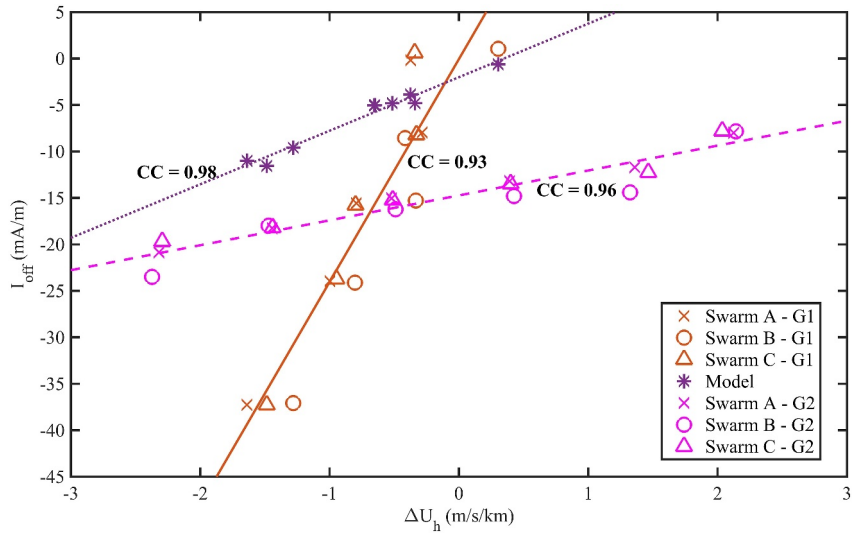

Figure 6. I_{off} over the ΔU_h for Swarm-ICON observations for different categories based on I_{off} (orange) and ΔU_h(magenta). The average EEJ sideband currents from Swarm A (cross symbol), B (circle symbol), and C (triangle symbol) in conjunction with ICON winds are shown for both groupings, G1 for those based on I_{off} and G2 for ΔU_h. The line represents the linear regression line and correlation coefficient, CC is also mentioned. Purple represents the same as magenta but from the model driven by G1 group-averaged ICON/MIGHTI data.

suggest two possible reasons for the fact that the magnitude of I_{off} for the physical model is usually smaller than the magnitude of I_{off} for the two lines representing data groupings. (a) As noted in Section 2, the procedure for removing the effects of Sq currents from the Swarm magnetic signal may tend to overestimate the strength of the sideband currents. (b) The winds and/or conductivities may have systematic variations with magnetic latitude that are not considered in the model and could increase the magnitude of I_{off}.

4. Discussion

To gain further insights we examine the importance of the neutral wind gradients at different altitudes using numerical experiments and discuss the limitations of individual observational conjunctions and the model results.

The daytime, low-latitude zonal ionospheric current density J_ϕ due to the electric field and zonal winds in the 80–400 km altitude can be expressed as follows (Richmond, 1973):

$$J_\phi = \sigma_P E_\phi + \sigma_P \left[\frac{\int_{s_1}^{s_2} \sigma_H ds}{\int_{s_1}^{s_2} \sigma_P ds}\right] E_\phi + \sigma_H B U_\phi - \sigma_H B \left[\frac{\int_{s_1}^{s_2} \sigma_P U_\phi ds}{\int_{s_1}^{s_2} \sigma_P ds}\right] \tag{2}$$

U_ϕ is the zonal wind, and E_ϕ is the eastward EEF. The integrals are along the magnetic field lines from foot points s_1 to s_2 at the bottom of the ionosphere. Here σ_P, σ_H, and U_ϕ are strongly height-dependent, while the magnitude of magnetic field $|B|$ varies little within the dynamo region. The first two terms on the right-hand side of Equation 2 represent the current density J_E due to electric field E_ϕ, and the last two terms are the zonal wind-driven current density J_W which are the focus of this study. It is evident from the equation that the current contribution due to wind is zero if the wind is a constant along the magnetic field line.

$$\text{Further,} \quad J_\phi = J_E + J_W \tag{3}$$

$$\text{Or} \quad J_\phi = J_E + \sigma_H B\left(U_\phi - \overline{U_\phi}\right) \tag{4}$$

$$\text{with } \overline{U_\phi} = \frac{\int_{s_1}^{s_2} \sigma_P U_\phi ds}{\int_{s_1}^{s_2} \sigma_P ds} \tag{5}$$

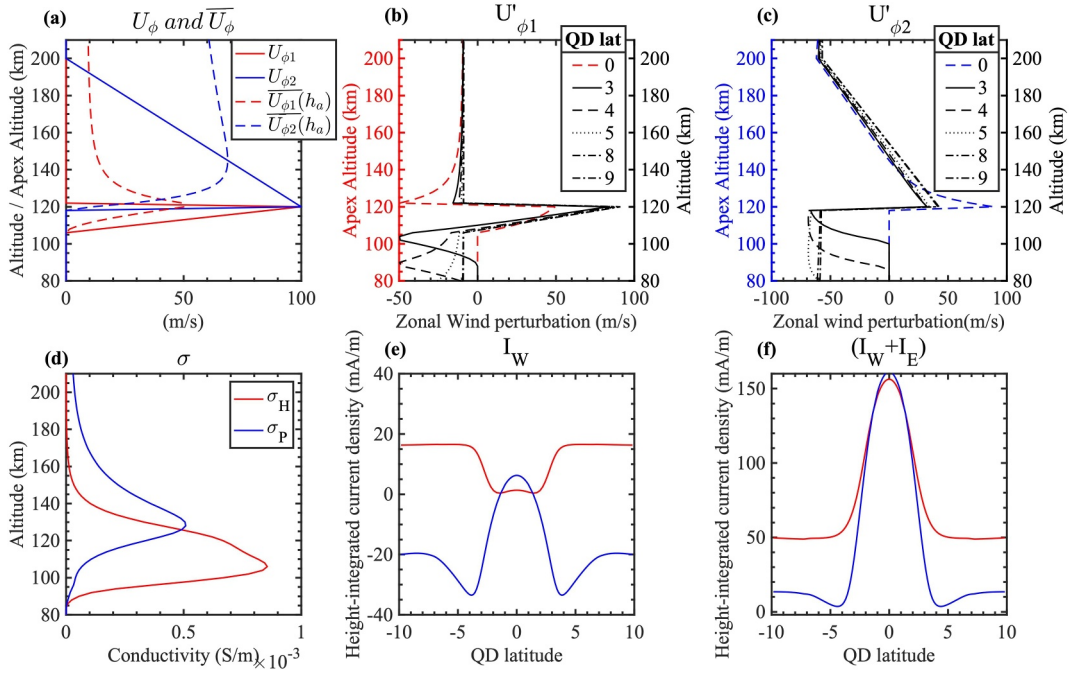

Figure 7. (a) Zonal winds ($U_{\phi1}$ and $U_{\phi2}$) with respect to altitude (h) and the average winds ($\overline{U_{\phi1}}(h_a)$ and $\overline{U_{\phi2}}(h_a)$) at magnetic equator with respect to apex altitude (h_a). (b and c) Altitudinal profile of the wind perturbations ($U'_{\phi1}$ and $U'_{\phi2}$) at magnetic latitudes 0, 3, 4, 5, 8, and 9° for the illustrative cases 1 and 2, respectively (d) Hall (σ_H) and Pedersen (σ_P) conductivities, (e) and (f) are height-integrated current density due to wind (I_W) alone, and both wind and electric field ($I_W + I_E$). Here red and blue color indicates the current densities for the illustrative cases 1 and 2, respectively.

being the field-line average zonal wind weighted by the Pedersen conductivity. By definition $\overline{U_\phi}$ is constant along a field line. We can define a perturbation wind as

$$U'_\phi = U_\phi - \overline{U_\phi} \tag{6}$$

Then,

$$J_W = \sigma_H B U'_\phi \tag{7}$$

Therefore, only the zonal wind perturbation with respect to the field-line average Pedersen conductivity weighted zonal wind matters in the determination of wind driven current density. In the magnetic equatorial region, the westward zonal winds at altitudes where Pedersen conductivity dominates (~130–180 km) builds an upward polarization electric field to balance the vertical/meridional Pedersen current. The equipotential nature of magnetic field lines leads to the mapping of this electric field to low-latitude E region and generates eastward Hall currents (Fang et al., 2008). When these wind effects get superimposed on the effect of the eastward EEF, we get a reduction in eastward current density at low-latitudes. These reduced eastward currents become westward in nature once the background currents are removed. Further, the height-integrated current density *I* considered for the analysis is estimated by integrating *J* over all altitudes.

In Figure 7a, we take two example wind profiles ($U_{\phi1}$ and $U_{\phi2}$) which are simplified from the ICON wind observations in C1 and split each into two altitude regions. Note that shifting the *x*-axis to the left or right is irrelevant since a constant wind in altitude does not generate any J_w as noted above. The wind profiles used are (a) $U_{\phi1}$ with positive eastward wind gradient in the Hall region (~106–120 km), and (b), $U_{\phi2}$ with negative eastward wind gradient in Pedersen region (~120–200 km). Both wind profiles have zero winds at altitudes other than the mentioned regions. The altitudinal variation of Hall and Pedersen conductivity is depicted in Figure 7d for reference. σ_H is dominant below 130 km while σ_P is dominant above.

Figure 7a also illustrates the field line averaged Pedersen conductivity weighted zonal winds (Equation 5), $\overline{U_\phi}$ over apex altitude h_a (equivalent to different field lines) using dashed lines. The perturbation winds $U'_{\phi 1}$ and $U'_{\phi 2}$ (Equation 6) are given in Figures 7b and 7c over altitude at particular QD latitudes for case 1 and 2, respectively.

For the wind profile $U_{\phi 1}$ (Figure 7a red solid curve), $U'_{\phi 1}$ at the equator (red dashed curve in Figure 7b) is positive below 120 km and negative in the 120–150 km range. This leads to a slightly positive or eastward I_W at the equator (Red curve in Figure 7e) since $U'_{\phi 1}$ is weighted by Hall conductivity. Even though sideband currents are generated by the neutral wind, these are too equatorward and not visible once I_E is added to I_W (Figure 7f). For increasing QD latitude, $U'_{\phi 1}$ is negative below 110 km and strongly positive in the 110–120 km altitudinal range, and almost constant negative above 120 km. The altitude integration of $U'_{\phi 1}$ weighted by Hall conductivity increases from QD latitude 3° to approximately 8°. Poleward of 8°, J_W becomes latitudinally independent.

For the wind profile $U_{\phi 2}$ (Figure 7a blue solid curve), $U'_{\phi 2}$ at QD latitude 0 (blue dashed curve in Figure 7c) is zero below 120 km and positive in the 120–150 km range. Hence, eastward winds will produce eastward Hall currents at the equator. Increasing in QD latitude $U'_{\phi 2}$ are westward below 120 km and eastward in the 120–150 km altitudes. The dip seen in I_W (Figure 7e blue curve) at ∼3.8° is generated by a minimum combining the Hall conductivity weighted westward $U'_{\phi 2}$ wind below 120 km with the Hall conductivity weighted eastward wind above 120 km (see Figure 7c: 3, 4, and 5° latitude). Poleward of QD latitude ∼7°, $U'_{\phi 2}$ is not changing since the apex altitude is large (above ∼200 km), leading to a constant westward I_W (Figure 7e, blue curve). Adding I_W to I_E the dips are still visible since they occur sufficiently far from the magnetic equator (Figure 7f).

In summary, the dips are prevalent if the winds are becoming more westward or less eastward with increasing height in the Pedersen region, generating sideband current away from the equator, which confirms the observational results in Figures 4–6.

5. Conclusions

The observations of Swarm and ICON conjunctions are used to examine the predictions of F76 and understand the effect of vertical shears of the zonal wind on low-latitude currents. The following summarizes the results from this study:

a. This is the first time observational evidence has been presented connecting the zonal wind shears with the low-latitude sideband currents. Although data for individual conjunctions of Swarm and ICON show considerable scatter, a consistent positive relation between the wind shear in the 130–180 km height range and the sideband current strength is found when the data are averaged in bins grouped by either of these two parameters.
b. The grouped and averaged data are correlated in a manner consistent with a linear relation between the wind shear and the sideband current, as is predicted by the physical model. The observations indicate that a persistent zonal wind altitude gradient in the Pedersen conductivity region of ∼−1 m/s/km can generate ∼−2.68 to −24 mA/m sideband current.
c. The study adds to the understanding of the effect of local winds on the low-latitude current. For individual conjunctions, a linear model can explain ∼9.61% of the sideband current strength in terms of the wind gradient. When the data are grouped according to wind shear and bin-averaged, ∼86.5%–92.2% of the sideband current variation (across Swarm satellites and across categories) can be explained by the average vertical gradient in the zonal wind.
d. Both the altitudinal gradient in zonal winds and the altitude at which the gradient is present control the sideband currents. Depending on the altitude at which the vertical shear in zonal winds is present, the sideband currents may or may not be present.
e. The physical EEJ model aligns quantitatively with the observations. It predicts a linear relation between the sideband current strength and the wind shear, with a ratio lying between the slopes of the regression lines obtained from the averaged data that are grouped either in terms of sideband current strength or wind shear. The model sideband currents are weaker (less negative) than those estimated from the Swarm observations. This difference could be due to biases in the estimation of sideband current strength from the Swarm magnetometer data, as well as simplifications in the model.

Data Availability Statement

The Swarm Level 2 product EEF (Alken, Maus, et al., 2013), including the equatorial electrojet intensity used in this study, can be downloaded at http://swarm-diss.eo.esa.int. The ICON/MIGHTI Level 2.2 product Cardinal Vector Winds (Version 4) (Harding et al., 2023) is accessible from the ICON website https://icon.ssl.berkeley.edu/Data and SPDF (https://spdf.gsfc.nasa.gov/data_orbits.html). The geomagnetic activity index Kp (Matzka et al., 2021) was provided by the GFZ German Research Centre for Geosciences (https://www.gfz-potsdam.de/en/section/geomagnetism/data-products-services/geomagnetic-kp-index). The F10.7 index (Tapping, 2013) can be downloaded from the SPDF OMNI- Web database https://ccmc.gsfc.nasa.gov/requests/GetInput/get_indices.php. EEJ model results can be accessed without any restriction via the zenodo general repository in Sreelakshmi et al. (2023).

Acknowledgments

We acknowledge the review provided by two anonymous reviewers, which contributed to the improvement of manuscript. JS and GV are supported by the Department of Science and Technology, Government of India. JS is also supported by NCAR/HAO Newkirk Graduate Research Fellowship. ICON is supported by NASA's Explorers Program through contracts NNG12FA45C and NNG12FA42I. AM is supported by ICON explorer NASA award 80NSSC221K1990. AM and PA are supported by USPI NASA award 80NSSC21K0449, Electrojet Zeeman Imaging Explorer (EZIE). This research was supported in part NOAA cooperative agreement NA22OAR4320151. The European Space Agency (ESA) is gratefully acknowledged for providing Swarm data. This material is based upon work supported by the National Center for Atmospheric Research, which is a major facility sponsored by the National Science Foundation under Cooperative Agreement No. 1852977. We would like to acknowledge the use of computational resources (https://doi.org/10.5065/D6RX99HX) at the NCAR-Wyoming Supercomputing Center provided by the National Science Foundation and the State of Wyoming, and supported by NCAR's Computational and Information Systems Laboratory.

References

Alken, P. (2020). Estimating currents and electric fields at low latitudes from satellite magnetic measurements. In M. W. Dunlop, & H. Lühr (Eds.), *Ionospheric multi-spacecraft analysis tools* (pp. 233–254). Springer International Publishing. https://doi.org/10.1007/978-3-030-26732-2_11

Alken, P., Chulliat, A., & Maus, S. (2013). Longitudinal and seasonal structure of the ionospheric equatorial electric field. *Journal of Geophysical Research: Space Physics*, *118*(3), 1298–1305. https://doi.org/10.1029/2012ja018314

Alken, P., Maus, S., Emmert, J., & Drob, D. P. (2008). Improved horizontal wind model HWM07 enables estimation of equatorial ionospheric electric fields from satellite magnetic measurements. *Geophysical Research Letters*, *35*(11), L11105. https://doi.org/10.1029/2008GL033580

Alken, P., Maus, S., Vigneron, P., Sirol, O., & Hulot, G. (2013). Swarm SCARF equatorial electric field inversion chain. *Earth Planets and Space*, *65*(11), 1309–1317. https://doi.org/10.5047/eps.2013.09.008

Anandarao, B. G., & Raghavarao, R. (1987). Structural changes in the currents and fields of the equatorial electrojet due to zonal and meridional winds. *Journal of Geophysical Research*, *92*(A3), 2514–2526. https://doi.org/10.1029/JA092iA03p02514

Cain, J. C., & Sweeney, R. E. (1973). The POGO data. *Journal of Atmospheric and Terrestrial Physics*, *35*(6), 1231–1247. https://doi.org/10.1016/0021-9169(73)90021-4

Chapman, S. (1956). The electrical conductivity of the ionosphere: A review. *Il Nuovo Cimento—B*, *4*(S4), 1385–1412. https://doi.org/10.1007/BF02746310

Deming, W. E. (1964). *Statistical adjustment of data (Unabridged and corr. republication)*. Dover Publications.

England, S. L., Englert, C. R., Harding, B. J., Triplett, C. C., Marr, K., Harlander, J. M., et al. (2022). Vertical shears of horizontal winds in the lower thermosphere observed by ICON. *Geophysical Research Letters*, *49*(11), e2022GL098337. https://doi.org/10.1029/2022GL098337

Englert, C. R., Harlander, J. M., Brown, C. M., Marr, K. D., Miller, I. J., Stump, J. E., et al. (2017). Michelson interferometer for global high-resolution thermospheric imaging (MIGHTI): Instrument design and calibration. *Space Science Reviews*, *212*(1–2), 553–584. https://doi.org/10.1007/s11214-017-0358-4

Englert, C. R., Harlander, J. M., Marr, K. D., Harding, B. J., Makela, J. J., Fae, T., et al. (2023). Michelson interferometer for global high-resolution thermospheric imaging (MIGHTI) on-orbit wind observations: Data analysis and instrument performance. *Space Science Reviews*, *219*(3), 27. https://doi.org/10.1007/s11214-023-00971-1

Fambitakoye, O., & Mayaud, P. N. (1976a). Equatorial electrojet and regular daily variation SR—I. A determination of the equatorial electrojet parameters. *Journal of Atmospheric and Terrestrial Physics*, *38*(1), 1–17. https://doi.org/10.1016/0021-9169(76)90188-4

Fambitakoye, O., & Mayaud, P. N. (1976b). Equatorial electrojet and regular daily variation SR—II. The centre of the equatorial electrojet. *Journal of Atmospheric and Terrestrial Physics*, *38*(1), 19–26. https://doi.org/10.1016/0021-9169(76)90189-6

Fambitakoye, O., Mayaud, P. N., & Richmond, A. D. (1976). Equatorial electrojet and regular daily variation SR—III. Comparison of observations with a physical model. *Journal of Atmospheric and Terrestrial Physics*, *38*(2), 113–121. https://doi.org/10.1016/0021-9169(76)90118-5

Fang, T. W., Richmond, A. D., Liu, J. Y., & Maute, A. (2008). Wind dynamo effects on ground magnetic perturbations and vertical drifts. *Journal of Geophysical Research*, *113*(A11), A11313. https://doi.org/10.1029/2008JA013513

Finlay, C. C., Kloss, C., Olsen, N., Hammer, M. D., Tøffner-Clausen, L., Grayver, A., & Kuvshinov, A. (2020). The CHAOS-7 geomagnetic field model and observed changes in the South Atlantic Anomaly. *Earth Planets and Space*, *72*(1), 156. https://doi.org/10.1186/s40623-020-01252-9

Forbes, J. M. (2007). Dynamics of the thermosphere. *Journal of the Meteorological Society of Japan. Series II*, *85B*, 193–213. https://doi.org/10.2151/jmsj.85B.193

Friis-Christensen, E., Lühr, H., & Hulot, G. (2006). Swarm: A constellation to study the Earth's magnetic field. *Earth Planets and Space*, *58*(4), 351–358. https://doi.org/10.1186/BF03351933

Hagan, M. E., & Forbes, J. M. (2002). Migrating and nonmigrating diurnal tides in the middle and upper atmosphere excited by tropospheric latent heat release. *Journal of Geophysical Research*, *107*(D24), ACL6-1–ACL6-15. https://doi.org/10.1029/2001JD001236

Harding, B. J., Chau, J. L., He, M., Englert, C. R., Harlander, J. M., Marr, K. D., et al. (2021). Validation of ICON-MIGHTI thermospheric wind observations: 2. Green-line comparisons to specular meteor radars. *Journal of Geophysical Research: Space Physics*, *126*(3), e2020JA028947. https://doi.org/10.1029/2020JA028947

Harding, B. J., Englert, C. R., Harlander, J. M., Marr, K. D., Makela, J. M., Brown, C. M., et al. (2023). ICON Michelson interferometer for global high-resolution thermospheric imaging wind vectors green [Dataset]. *NASA Space Physics Data Facility*. https://doi.org/10.48322/VTCE-7Y29

Harding, B. J., Makela, J. J., Englert, C. R., Marr, K. D., Harlander, J. M., England, S. L., & Immel, T. J. (2017). The MIGHTI wind retrieval algorithm: Description and verification. *Space Science Reviews*, *212*(1–2), 585–600. https://doi.org/10.1007/s11214-017-0359-3

Immel, T. J., England, S. L., Mende, S. B., Heelis, R. A., Englert, C. R., Edelstein, J., et al. (2018). The ionospheric connection explorer mission: Mission goals and design. *Space Science Reviews*, *214*(1), 13. https://doi.org/10.1007/s11214-017-0449-2

Jadhav, G., Rajaram, M., & Rajaram, R. (2002). A detailed study of equatorial electrojet phenomenon using Ørsted satellite observations: Techniques. *Journal of Geophysical Research*, *107*(A8), SIA12-1–SIA12-12. https://doi.org/10.1029/2001JA000183

Lühr, H., Maus, S., & Rother, M. (2004). Noon-time equatorial electrojet: Its spatial features as determined by the CHAMP satellite. *Journal of Geophysical Research*, *109*(A1), A01306. https://doi.org/10.1029/2002JA009656

Lühr, H., Zhou, Y. L., & Alken, P. (2021). Short-term variability of equatorial electrojet modulation by solar tidal and planetary waves, as derived from the Swarm constellation. *Journal of Geophysical Research: Space Physics*, *126*(5), e2020JA028884. https://doi.org/10.1029/2020ja028884

Manoj, C., Lühr, H., Maus, S., & Nagarajan, N. (2006). Evidence for short spatial correlation lengths of the noontime equatorial electrojet inferred from a comparison of satellite and ground magnetic data. *Journal of Geophysical Research*, *111*(A11), A11312. https://doi.org/10.1029/2006JA011855

Matzka, J., Stolle, C., Yamazaki, Y., Bronkalla, O., & Morschhauser, A. (2021). The geomagnetic *Kp* index and derived indices of geomagnetic activity. *Space Weather*, *19*(5), e2020SW002641. https://doi.org/10.1029/2020SW002641

Maute, A., & Richmond, A. D. (2017). Examining the magnetic signal due to gravity and plasma pressure gradient current with the TIE-GCM. *Journal of Geophysical Research: Space Physics*, *122*(12), 12486–12504. https://doi.org/10.1002/2017JA024841

Olsen, N., Friis-Christensen, E., Floberghagen, R., Alken, P., Beggan, C. D., Chulliat, A., et al. (2013). The Swarm satellite constellation application and research facility (SCARF) and Swarm data products. *Earth Planets and Space*, *65*(11), 1189–1200. https://doi.org/10.5047/eps.2013.07.001

Onwumechili, C. A. (1992). Study of the return current of the equatorial electrojet. *Journal of Geomagnetism and Geoelectricity*, *44*(1), 1–42. https://doi.org/10.5636/jgg.44.1

Reddy, C. A., & Devasia, C. V. (1981). Height and latitude structure of electric fields and currents due to local east-west winds in the equatorial electrojet. *Journal of Geophysical Research*, *86*(A7), 5751–5767. https://doi.org/10.1029/JA086iA07p05751

Richmond, A. D. (1972). *Numerical model of the equatorial electrojet*. Air Force Cambridge Research Laboratories, Office of Aerospace Research.

Richmond, A. D. (1973). Equatorial electrojet—I. Development of a model including winds and instabilities. *Journal of Atmospheric and Terrestrial Physics*, *35*(6), 1083–1103. https://doi.org/10.1016/0021-9169(73)90007-X

Riggs, D. S., Guarnieri, J. A., & Addelman, S. (1978). Fitting straight lines when both variables are subject to error. *Life Sciences*, *22*(13–15), 1305–1360. https://doi.org/10.1016/0024-3205(78)90098-X

Shepherd, G. G., Thuillier, G., Cho, Y.-M., Duboin, M.-L., Evans, W. F. J., Gault, W. A., et al. (2012). The wind imaging interferometer (WINDII) on the upper atmosphere research satellite: A 20 year perspective: The wind imaging interferometer (WINDII). *Reviews of Geophysics*, *50*(2), RG2007. https://doi.org/10.1029/2012RG000390

Shepherd, G. G., Thuillier, G., Gault, W. A., Solheim, B. H., Hersom, C., Alunni, J. M., et al. (1993). WINDII, the wind imaging interferometer on the upper atmosphere research satellite. *Journal of Geophysical Research*, *98*(D6), 10725–10750. https://doi.org/10.1029/93JD00227

Sreelakshmi, J., Maute, A., Richmond, A. D., Vichare, G., Harding, B. J., & Alken, P. (2023). Effect of vertical shear in the zonal wind on equatorial electrojet sidebands: An observational perspective using Swarm and ICON data [Dataset]. *Zenodo*. https://doi.org/10.5281/ZENODO.7639973

Sreelakshmi, J., & Vichare, G. (2020). Gravity and pressure-gradient currents using ionospheric electron density measurements from COSMIC satellites. *Journal of Geophysical Research: Space Physics*, *125*(10), e2020JA028401. https://doi.org/10.1029/2020JA028401

Stening, R. J. (1995). What drives the equatorial electrojet? *Journal of Atmospheric and Terrestrial Physics*, *57*(10), 1117–1128. https://doi.org/10.1016/0021-9169(94)00127-A

Tapping, K. F. (2013). The 10.7 cm solar radio flux (F10.7): F10.7. *Space Weather*, *11*(7), 394–406. https://doi.org/10.1002/swe.20064

Thomas, N., Vichare, G., & Sinha, A. K. (2017). Characteristics of equatorial electrojet derived from Swarm satellites. *Advances in Space Research*, *59*(6), 1526–1538. https://doi.org/10.1016/j.asr.2016.12.019

Vichare, G., Bhaskar, A., & Ramesh, D. S. (2016). Are the equatorial electrojet and the Sq coupled systems? Transfer entropy approach. *Advances in Space Research*, *57*(9), 1859–1870. https://doi.org/10.1016/j.asr.2016.01.020

Witte, R. S., & Witte, J. S. (2017). *Statistics*. John Wiley & Sons. Retrieved from https://books.google.co.in/books?hl=en&lr=&id=KcxjDwAAQBAJ&oi=fnd&pg=PA1&ots=d3sXT6eO8v&sig=LrWRiyYMUGRpD0o4WUIfiG-WzUc&redir_esc=y#v=onepage&q&f=false

Yamazaki, Y., Harding, B. J., Stolle, C., & Matzka, J. (2021). Neutral wind profiles during periods of eastward and westward equatorial electrojet. *Geophysical Research Letters*, *48*(11), e2021GL093567. https://doi.org/10.1029/2021GL093567

Yamazaki, Y., & Maute, A. (2017). Sq and EEJ—A review on the daily variation of the geomagnetic field caused by ionospheric dynamo currents. *Space Science Reviews*, *206*(1–4), 299–405. https://doi.org/10.1007/s11214-016-0282-z

Yamazaki, Y., Stolle, C., Matzka, J., Siddiqui, T. A., Lühr, H., & Alken, P. (2017). Longitudinal variation of the lunar tide in the equatorial electrojet: Lunar tide. *Journal of Geophysical Research: Space Physics*, *122*(12), 12445–12463. https://doi.org/10.1002/2017JA024601

Zhou, Y.-L., Lühr, H., & Alken, P. (2018). The sidebands of the equatorial electrojet: General characteristic of the westward currents, as deduced from CHAMP. *Journal of Geophysical Research: Space Physics*, *123*(2), 1457–1476. https://doi.org/10.1002/2017JA024687